



In situ synthesis of C-TiO₂/g-C₃N₄ heterojunction nanocomposite as highly visible light active photocatalyst originated from effective interfacial charge transfer



Zhao Lu^a, Lei Zeng^c, Wulin Song^{a,b,*}, Ziyu Qin^a, Dawen Zeng^a, Changsheng Xie^a

^a State Key Laboratory of Materials Processing and Die & Mould Technology, Huazhong University of Science and Technology, 1037 Luoyu Road, Wuhan 430074, PR China

^b Analytical and Testing Center of Huazhong University of Science and Technology, Wuhan 430074, PR China

^c South University of Science and Technology of China, 1088 Xueyuan Road, Shenzhen 518055, PR China

ARTICLE INFO

Article history:

Received 14 June 2016

Received in revised form 16 August 2016

Accepted 24 September 2016

Available online 27 September 2016

Keywords:

Visible light photocatalyst

C–Ti bond

N–Ti bond

Effective interfacial charge transfer

ABSTRACT

In this paper, a simple one-pot hydrothermal strategy was adopted to prepare C-TiO₂/g-C₃N₄ nanocomposite. Simultaneously, the photocatalytic performance of the C-TiO₂/g-C₃N₄ nanocomposite like tunable ratio was evaluated by the degradation of methyl orange (MO) under visible light irradiation. The prepared nanocomposite with the mass ratio of 27:8 (C-TiO₂/g-C₃N₄(0.08)) possessed the highest photocatalytic activity, about 5.1, 3.8 and 2.3 times higher than that of C-TiO₂, g-C₃N₄, and the Mixing sample, respectively. The excellent photocatalytic performance was attributed to the improvement of light harvesting and charge separation caused by construction of heterojunction. In addition, interfacial charge transfer through C–Ti bond and N–Ti bond also played a crucial role in inhibiting the recombination of electron–hole pairs and increasing the concentrations of holes and electrons, separately, which was confirmed by XPS analysis, photocurrent response experiment, electrochemical impedance spectroscopy measurements, PL spectra and Time-resolved PL spectra. Besides, the importance of active species during the reaction process was explored, and the generation of h⁺, O₂[–], OH in the photocatalytic process was also demonstrated. Among this, O₂[–] played an important role. This finding about chemically bonded C-TiO₂/g-C₃N₄ nanocomposite provided a good guidance for the fabrication of new heterogeneous photocatalysts and facilitated their applications in environmental protection, water splitting and so on.

© 2016 Elsevier B.V. All rights reserved.

1. Introduction

With improvements in science, photocatalysis technique has been considered to be a desired strategy for environmental remediation due to its low-cost, environmental benefit, nontoxicity and stability [1–4]. TiO₂ based nanomaterials have attracted considerable attention since Fujishima and Honda first reported the photoelectrochemical splitting of water on a TiO₂ semiconductor electrode in 1972 [5]. However, the problems including low efficiency in solar energy utilization and rapid recombination of photogenerated electron–hole pairs within TiO₂ hinder its practical application. Over the past few decades, various modification strategies have been developed to extend the photo-response range and

improve the photocatalytic performance [6–9]. In particular, coupling with narrow band-gap semiconductor is considered to be an effective method which can improve the separation efficiency of photogenerated electron–hole pairs in the photocatalytic process, such as BiOBr [10], CdS [11], Cu₂O [12], Ag₂O [13] and so on.

Recently, TiO₂/g-C₃N₄ nanocomposite has become a hotspot in the field of photocatalysis due to the enhancement of photocatalytic activity induced by the construction of heterojunction. Gu et al. prepared g-C₃N₄/TiO₂ hybrid, and enhancement of visible light photocatalytic activity over the hybrid was achieved [14]. Chen et al. investigated the visible-light photocatalytic performance of heterostructured g-C₃N₄/Ag/TiO₂ microspheres, and it showed significant photocatalytic activity [15]. The composite material comprising of doped TiO₂ and g-C₃N₄ has also attracted the researchers' attention, since it possesses the stronger visible light harvesting ability. Zhou et al. synthesized g-C₃N₄@N-TiO₂ heterojunction, and it exhibited enhanced photocatalytic performance for the selective photoreduction of CO₂ to CO [16]. Sridharan et al. found the improved photocatalytic activity in C and N co-doped

* Corresponding author at: State Key Laboratory of Materials Processing and Die & Mould Technology, Huazhong University of Science and Technology, 1037 Luoyu Road, Wuhan 430074, PR China.

E-mail address: wulins@126.com (W. Song).

$\text{TiO}_2/\text{g-C}_3\text{N}_4$ was owing to the formation of a synergistic heterojunction [17]. However, the effect of chemically bonded interface between TiO_2 and $\text{g-C}_3\text{N}_4$ on photocatalytic performance has been rarely reported.

In this paper, we report that a simple hydrothermal strategy is adopted to prepare $\text{C-TiO}_2/\text{g-C}_3\text{N}_4$ nanocomposite with chemically bonded interface through C–Ti bond and NTi bond, which is confirmed by XPS analysis. Compared with the Mixing sample, the chemically bonded $\text{C-TiO}_2/\text{g-C}_3\text{N}_4$ nanocomposite has higher separation efficiency of photogenerated electron-hole pairs, which is confirmed by the photocurrent response experiment, electrochemical impedance spectroscopy measurements, PL spectra and Time-resolved PL spectra. Hence, the chemically bonded $\text{C-TiO}_2/\text{g-C}_3\text{N}_4$ nanocomposite exhibits an excellent visible light photocatalytic activity. Our work develop a simple method to prepare a kind of nanocomposites with effective interfacial charge transfer through chemical bond and provide theoretical basis for further studies.

2. Experimental

2.1. Materials

All chemicals applied in this experiment including tetra-*n*-butyl titanate (TTIP, 98%; Sinopharm Chemical Reagent Co., Ltd.), urea, ethylene glycol (EG) and ethanol were purchased and used without any further purification. High-purity deionized water was used throughout all experiments.

2.2. Synthesis of $\text{g-C}_3\text{N}_4$

The $\text{g-C}_3\text{N}_4$ power was prepared by the thermal polycondensation of urea. In retail, 10 g of urea was put into a ceramic crucible with a cover, heated at 550 °C for 4 h with a temperature rise rate at 15 °C/min in a muffle furnace. After cooling to room temperature naturally, the resulting pale yellow products were collected and ground into powders.

2.3. Preparation of pure TiO_2 and C-TiO_2

The pure TiO_2 and carbon-doped TiO_2 (C-TiO_2) were both prepared according to hydrothermal method. For the C-TiO_2 , in a typical procedure, 1 mL TTIP was firstly dissolved in 40 mL EG at room temperature. Then, the above solution was added dropwise to the 40 mL deionized water under vigorous stirring for 30 min. Next, the final suspension solution was transferred into a 100 mL Teflon-lined autoclave, and maintained at 180 °C for 12 h. After cooling to ambient temperature naturally, the resulting product was centrifuged and rinsed with absolute ethanol and distilled water for several cycles to remove residual EG on the surface. The obtained precipitate was dried at 80 °C in a vacuum oven. The pure TiO_2 was also obtained through the same process only without using EG.

2.4. Preparation of $\text{C-TiO}_2/\text{g-C}_3\text{N}_4$ nanocomposite

The $\text{C-TiO}_2/\text{g-C}_3\text{N}_4$ was also synthesized by hydrothermal method. At first, a certain amount of $\text{g-C}_3\text{N}_4$ was added to 40 mL distilled water under vigorous magnetic stirring for 1 h to form solution A. Likewise, 1 mL TTIP was dissolved in 40 mL EG at room temperature to form solution B. Then, solution B was added dropwise to solution A under vigorous stirring for 30 min. Afterwards, the mixed solution was transferred into a 100 mL Teflon-lined autoclave to react at 180 °C for 10 h. At last, the resulting product was centrifuged and washed with absolute ethanol and distilled water, and dried in a vacuum oven at 80 °C overnight to get the $\text{C-TiO}_2/\text{g-C}_3\text{N}_4$ nanocomposite. By varying the dosage of $\text{g-C}_3\text{N}_4$ at 0.02, 0.04,

0.06, 0.08 and 0.1 g, a series of $\text{C-TiO}_2/\text{g-C}_3\text{N}_4$ nanocomposites were synthesized, labeled as $\text{C-TiO}_2/\text{g-C}_3\text{N}_4(0.02)$, $\text{C-TiO}_2/\text{g-C}_3\text{N}_4(0.04)$, $\text{C-TiO}_2/\text{g-C}_3\text{N}_4(0.06)$, $\text{C-TiO}_2/\text{g-C}_3\text{N}_4(0.08)$ and $\text{C-TiO}_2/\text{g-C}_3\text{N}_4(0.1)$, respectively. For comparison, a mixing sample with some mass ratios of $\text{g-C}_3\text{N}_4$ to C-TiO_2 to $\text{C-TiO}_2/\text{g-C}_3\text{N}_4(0.08)$ was prepared by a simple mechanical mixing of C-TiO_2 and $\text{g-C}_3\text{N}_4$, which was noted hereafter as “Mixing”.

2.5. Characterization

The crystal phases of all samples were characterized by X-ray diffraction (PANalytical B.V., Almelo, the Netherlands) with a $\text{Cu K}\alpha$ radiation, and their microstructures were observed by high-resolution transmission electron microscopy (HRTEM, FEI Tecnai G2 F30 field-emission TEM). Fourier transform infrared (FT-IR) spectra were recorded from a KBr disk on the FT-IR Bruker Tensor27. Chemical composition and valence band (VB) were detected by X-ray photoelectron spectroscopy (XPS) measurements in a VG Multilab2000 spectrometer. UV-vis diffuse reflectance spectroscopy (UV-vis DRS) absorption spectra were recorded at a Shimadzu U-3010 spectrometer using BaSO_4 as a reference. Photoluminescence (PL) spectra of these powders were obtained on a Jasco FP-6500 with a laser excitation of 325 nm. Time-resolved PL decay (TRPL) spectroscopy was detected by a fluorescence spectrometer (F900) with an excitation wavelength of 375 nm. And the signals collected at excitation wavelength of 500 nm. ESR signals of $\cdot\text{O}_2^-$ and $\cdot\text{OH}$ with 5, 5-diethyl-1-pyrroline N-oxide (DMPO) were recorded with a Bruker A300-10/12 ESR spectrometer.

The electrochemical impedance spectroscopy measurements (EIS) were carried out on a Shanghai Chenhua CHI-660D electrochemical system by using a conventional three-electrode cell. The electrolyte solution was 0.1 M Na_2SO_4 . The counter and the reference electrodes were platinum wire and saturated calomel electrode (SCE), respectively. The as-prepared photocatalyst powders were fixed to the film electrodes by the following method: First, 10 mg catalyst sample was mixed with 1 mL distilled water homogeneously (10 mg/mL). Then the solution was spin-coated onto an ITO glass electrode. At last, the electrode was dried naturally for 12 h and then dried at 120 °C for 5 h.

2.6. Photocatalytic activity test

The photocatalytic activities were evaluated by measuring the degradation of methyl orange (MO) in an aqueous solution under visible light irradiation ($\lambda > 400$ nm). In order to keep the temperature of MO solution maintained at room temperature, a liquid trap system with water circulation facility was used. A 300 W Xe lamp (CEL-HXF300) with a UV-cutoff filter as visible light source was put 15 cm over the liquid trap system. Generally, 50 mg catalyst was well dispersed in 50 mL MO solution of 20 mg/L. Before photocatalytic experiments, the reaction suspensions were vigorously stirred for 30 min to ensure the absorption-desorption equilibrium of the MO on the catalyst surface. At a given time interval, 5 mL samples were taken from the suspensions and centrifuged. Then, the supernatant fluid was extracted immediately. The concentration of MO was analyzed by UV/vis spectroscopy. The degradation rate was calculated by C/C_0 , where C was the concentration of MO in each time period, and C_0 was the concentration of MO after dark adsorption. A blank control test without photocatalyst was performed for reference.

To identify the generated active species during the reaction process, ammonium oxalate (AO), 1, 4-benzoquinone (BQ) and 2-propanol (IPA) were used as the hole (h^+) scavenger, superoxide radical ($\cdot\text{O}_2^-$) scavenger and hydroxyl radical ($\cdot\text{OH}$) scavenger, respectively. A proper amount of scavenger was added to the MO

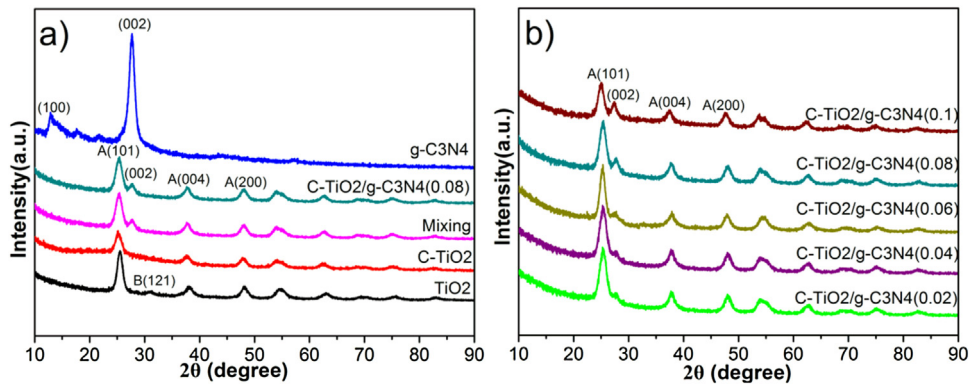


Fig. 1. XRD patterns of all samples.

solution to probe the active species through variation of degradation rate.

3. Results and discussion

3.1. XRD characterization

Fig. 1 shows the XRD patterns of all samples. From Fig. 1a, it is obvious that the pure TiO₂ sample can be indexed to the anatase (JCPDS file No. 21-1272) and brookite (JCPDS file No. 03-0380). However, the peak around 30° which is mainly indexed to brookite disappears and the main peaks shift to lower value in C-TiO₂, it suggests that carbon atom has been incorporated into the TiO₂ successfully [18,19]. Meanwhile, it can be also found the crystal size of anatase decreases after carbon doping by comparing the (101) peak in Fig. 1a. The XRD pattern of g-C₃N₄ clearly has two characteristic diffraction peaks at 13.05° (100) and 27.47° (002) which are attributed to the in-plane structure of tri-s-triazine units and the interlayer stacking of the conjugated aromatic groups, respectively [20,21]. For the C-TiO₂/g-C₃N₄(0.08), the intensity of peak referred to g-C₃N₄ decreases, it may be due to the relatively low amount. Similarly, the feature peaks of g-C₃N₄ and C-TiO₂ phases are detectable in the Mixing sample, indicating that the phase composition of the Mixing sample is same to that of C-TiO₂/g-C₃N₄(0.08). As displayed in Fig. 1b, the peaks of C-TiO₂ and g-C₃N₄ are clearly observed in all C-TiO₂/g-C₃N₄ nanocomposites, but the intensity of peak (002) increases as the increase of the mass of g-C₃N₄, this is supposed to be caused by the variation of mass ratios of g-C₃N₄ to C-TiO₂.

3.2. TEM characterization

Fig. 2 shows the microstructures of as-prepared samples and elemental compositions of C-TiO₂/g-C₃N₄(0.08). As shown in Fig. 2a, g-C₃N₄ has a wrinkle sheet-like structure and the surface is not really smooth. Compared with TiO₂, the grain size of the C-TiO₂ is relatively small, which is accord with the results of XRD. HRTEM images inserted in Fig. 2 show clear lattice fringes of TiO₂ and C-TiO₂. The lattice of 0.35 nm corresponds to the (101) planes of the TiO₂ and C-TiO₂. After adding g-C₃N₄ in hydrothermal reaction, the C-TiO₂ particles are well dispersed on the g-C₃N₄ in C-TiO₂/g-C₃N₄(0.08), furthermore, the phase structure and particle size of C-TiO₂ both have no significant change. Similar to the C-TiO₂/g-C₃N₄(0.08), C-TiO₂ particles are also located on g-C₃N₄ nanosheet in the Mixing sample as shown in Fig. 2e, but the distribution of C-TiO₂ particles is non-uniform. Elemental compositions of the C-TiO₂/g-C₃N₄(0.08) is analyzed by EDX spectra. As shown in Fig. 2f, the signals from C, N, Ti and O elements are detected.

Furthermore, a detailed chemical analysis was carried out using element mappings as shown in Fig. 3. It is clearly seen that the distribution of O element is consistent with its compositional element Ti, the C element is distributed across the whole surface, demonstrating that C element exists in the TiO₂. Meanwhile, C element distribution is generally same with that of the compositional element N, which is assigned to the g-C₃N₄ nanosheets. This result also indirectly indicates that C-TiO₂ particles are successfully incorporated with the g-C₃N₄ nanosheets.

3.3. FT-IR spectra

The local structures of all samples were investigated by FT-IR as shown in Fig. 4. For the pure TiO₂, it can be seen that a band at 400–800 cm⁻¹ is clearly shown in the FT-IR spectrum of TiO₂, which corresponds to the Ti—O—Ti stretching vibration [15,22,23]. Compared with TiO₂, an additional absorption band near 1084 cm⁻¹ can be found in C-TiO₂ which is associated with C—O stretching, indicating that carbon atom has been incorporated into the lattice of TiO₂ and the formation of Ti—O—C group. As for g-C₃N₄, there are three characteristic bands: the absorption band at 1638 cm⁻¹ is attributed to C—N stretching vibration; the strong band at 1200–1600 cm⁻¹ is associated with the typical aromatic C—N stretching vibration; the band near 810 cm⁻¹ is related to out-of plane bending modes of C—N heterocycles [24–26]. For the Mixing sample and all C-TiO₂/g-C₃N₄ nanocomposites, all the FT-IR bands for C-TiO₂ and g-C₃N₄ are basically retained. This demonstrates that C-TiO₂ and g-C₃N₄ both exists in the Mixing sample and all C-TiO₂/g-C₃N₄ nanocomposites, which accords well with the result of XRD.

3.4. Chemical compositions

To study the chemical composition and interaction between g-C₃N₄ and C-TiO₂, XPS analysis was utilized, as shown in Fig. 5.

Fig. 6a shows the high resolution XPS spectra of C 1s region. The binding energy of 284.8 eV is a typical peak position for adventitious carbon contamination adsorbed from the ambient environment, which cannot be eliminated. Furthermore, the deconvoluted peaks centered at the binding energy of 286.1 and 288.7 eV are attributed to the C—O and C=O oxygen-containing carbonaceous bands, severally [27,28]. C 1s spectra for C-TiO₂ is shown in Fig. 6b, the intensity of the peak at 286.1 eV increases obviously, indicating that the C—O bond forms in C-TiO₂, that is, carbon atoms incorporate into interstitial positions of the TiO₂ lattice, which is coincident with the result of FT-IR [29]. For the C-TiO₂/g-C₃N₄(0.08) nanocomposite, the peak at 288.1 eV can be distinguished for g-C₃N₄, which is assigned to sp²-hybridized carbon in the unit of (N)₂—C=N [30]. In addition, an additional peak located at 282.5 eV is very close to the

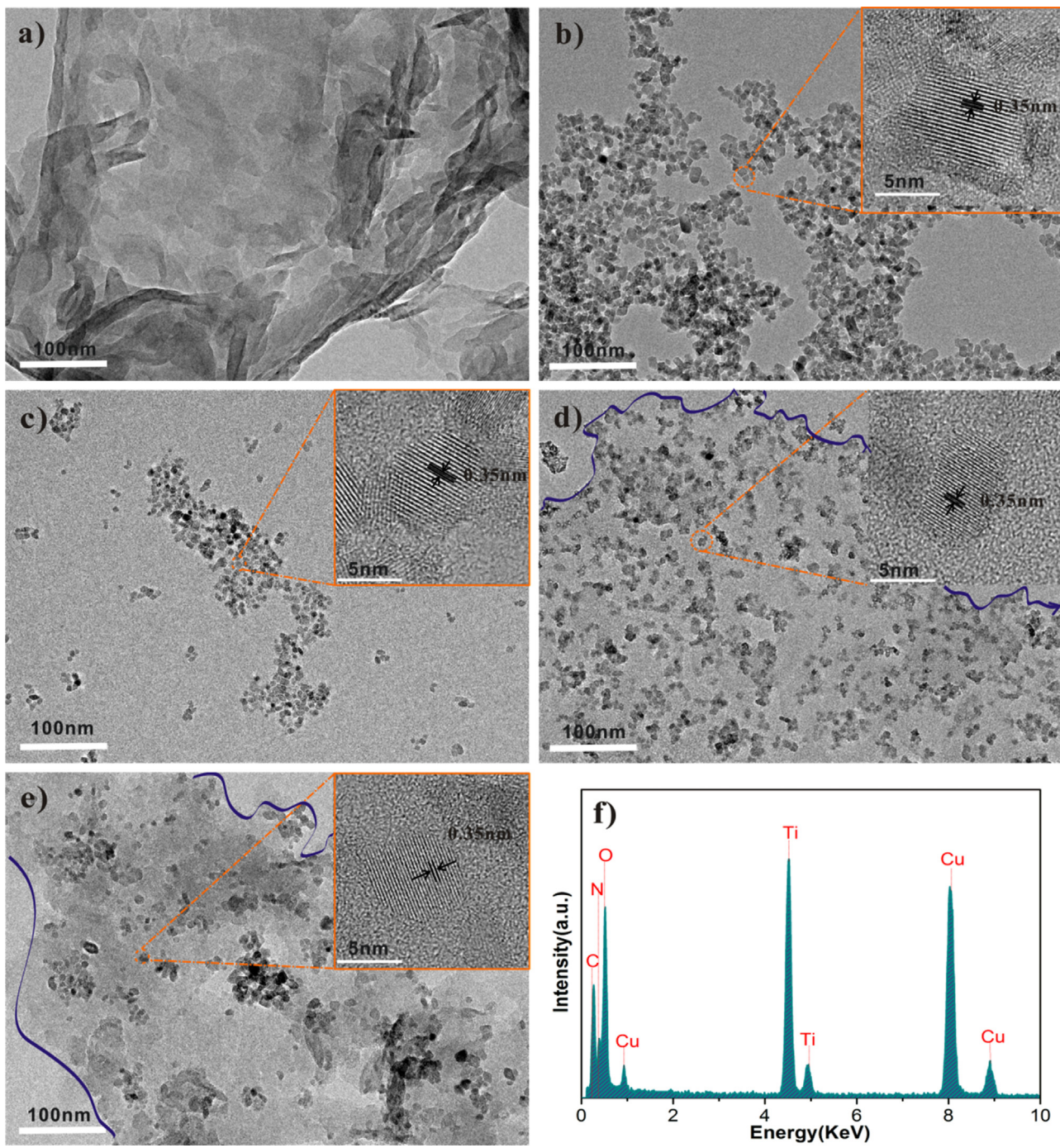


Fig. 2. TEM and HRTEM images of (a) g-C₃N₄, (b) TiO₂, (c) C-TiO₂, (d) C-TiO₂/g-C₃N₄(0.08), (e) the Mixing sample and (f) EDX spectra of C-TiO₂/g-C₃N₄(0.08).

C 1 s peak of TiC, which could be due to the formation of a chemical bond between the carbon atoms in g-C₃N₄ and the titanium atoms in the lattice of C-TiO₂ [28,31–33]. However, only the corresponding bonds for C-TiO₂ and g-C₃N₄ are retained in the Mixing sample as shown in Fig. 6d.

Fig. 7 shows the high resolution XPS spectra of N 1s region for C-TiO₂/g-C₃N₄(0.08) (a) and the Mixing sample (b). For the C-TiO₂/g-C₃N₄(0.08) in Fig. 7a, there are three characteristic peaks corresponding to the g-C₃N₄, the peak at 398.5 eV is attributed to C=N=C group, while the other two peaks at 399.6 and 400.9 eV can be assigned to N-(C)₃ and N–H groups [34]. Meanwhile, an additional peak at 396.1 eV appears in C-TiO₂/g-C₃N₄(0.08), which is usually assigned to the N–Ti bonding in this binding energy region

[35–37]. Combined with the results and analysis of C 1s region, it suggests that there is an interaction between the g-C₃N₄ and the C-TiO₂ resulting from C–Ti bond and N–Ti bond. Thus, it indicates that the double-bond of N=C has been broken, nitrogen atom and carbon atom both bond with titanium atom, which results in the formation of N–Ti–C group. In Comparison with C-TiO₂/g-C₃N₄(0.08), only three peaks attributed to g-C₃N₄ exist in the Mixing sample as shown in the Fig. 7b.

As shown in Fig. 8, formation of the C–Ti bond and N–Ti bond in the C-TiO₂/g-C₃N₄(0.08) also can be further examined and confirmed by analysis of the Ti 2p core level of the XPS. For the pure TiO₂, the Ti 2p_{3/2} and Ti 2p_{1/2} centering at 458.8 eV and 464.5 eV are found respectively, which are assigned to Ti–O bond [29]. After

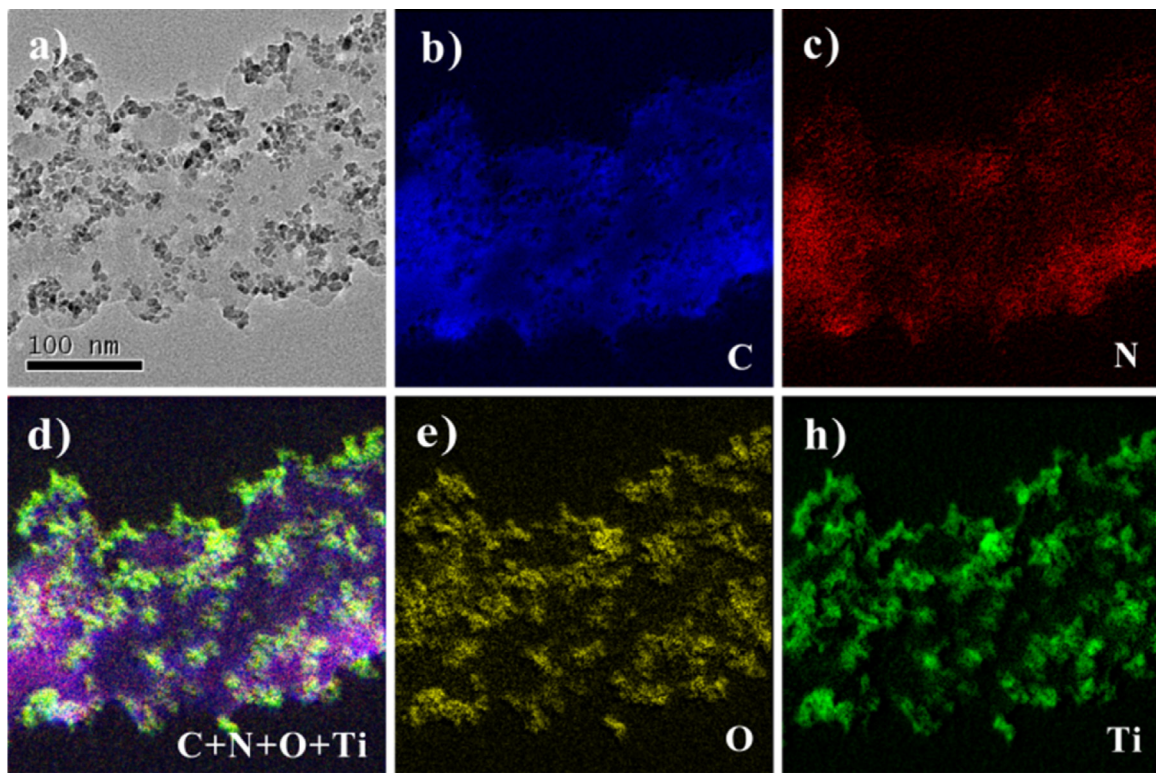


Fig. 3. TEM images of C-TiO₂/g-C₃N₄(0.08): (a) TEM image; (b) C element map; (c) N element map; (d) multi-elemental image of C, O, N and Ti; (e) O element map; (f) Ti element map.

carbon doping, it is evident that only these two peaks which are also attributed to Ti–O bond appear, without other bonds exist. Hence, it is suggested that carbon atoms are doped into the interstitial positions of TiO₂ lattice. In Fig. 8c, in addition to the two characteristic peaks of TiO₂ at 458.8 (Ti 2p3/2) and 464.5 eV (Ti 2p1/2), another two peaks centered at 455.2 and 460.8 eV can be found and result from C–Ti bond [32,33], and the rest of peaks at 462.1 and 456.9 eV which are attributed to N–Ti bond [35]. But it is easy to observe that just two peaks at 458.8 and 464.5 eV can be assigned to Ti–O bond for the Mixing sample as shown in Fig. 8d. This demonstrates that the C–Ti bond and N–Ti bond are present in the C-TiO₂/g-C₃N₄(0.08).

Combined with the above analysis, two additional bond (C–Ti bond and N–Ti bond) are formed in the C-TiO₂/g-C₃N₄(0.08), it

indicates that the C-TiO₂ nanoparticles are chemically bonding with the g-C₃N₄ nanosheets in C-TiO₂/g-C₃N₄(0.08).

3.5. UV-vis diffuse reflection spectra

Fig. 9 shows the UV-vis spectra of all samples. It is obvious that the modified samples show significant red-shifts compared with pure TiO₂. For C-TiO₂, the existence of trailing is the characteristic of element doped TiO₂, implying that carbon atoms have incorporated into the lattice of TiO₂, which is consistent with the result of XPS. For g-C₃N₄, the absorption spectrum is cut off at 450 nm. The synergistic effect is apparently shown in all C-TiO₂/g-C₃N₄ nanocomposites, revealing that the advantage of single material still remains in every nanocomposite. It is obvious that the visible

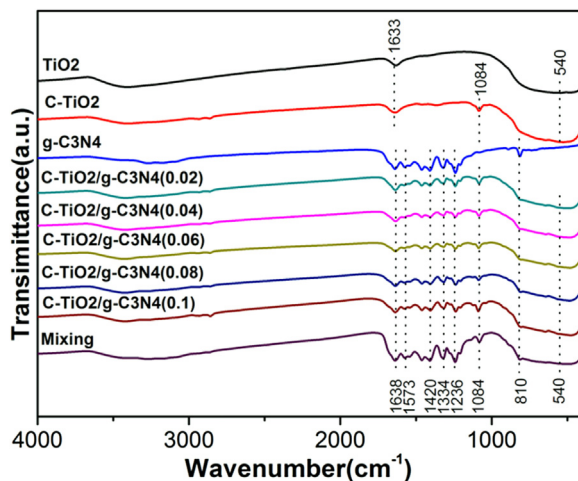


Fig. 4. FT-IR patterns of all samples.

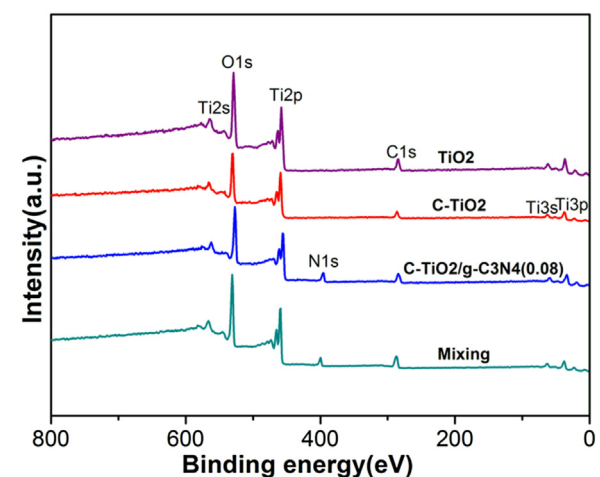


Fig. 5. XPS spectra: survey spectrum.

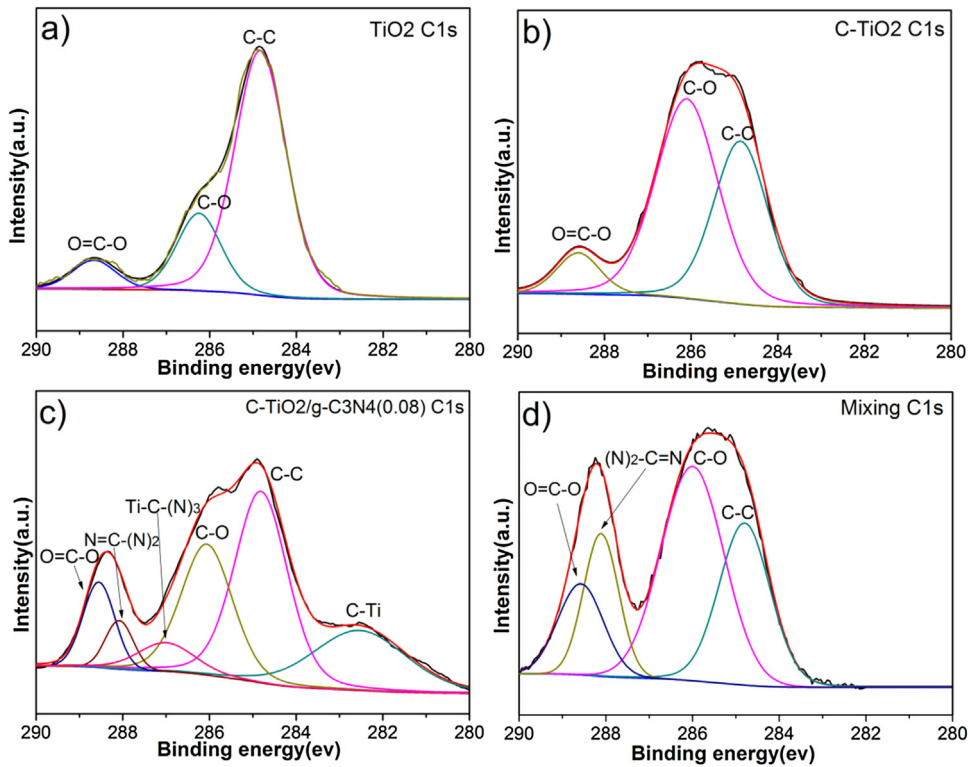


Fig. 6. C 1s XPS spectra of TiO₂ (a), C-TiO₂ (b), C-TiO₂/g-C₃N₄(0.08) (c) and the Mixing sample (d).

absorption ability of the Mixing sample is better than that of C-TiO₂, but it is worse than that of C-TiO₂/g-C₃N₄(0.08). As shown in Fig. 9b, C-TiO₂/g-C₃N₄(0.08) exhibits the strongest visible light absorption from 400 nm to 700 nm and the trailing effect also exists.

To further research the band structure of C-TiO₂/g-C₃N₄ nanocomposite, the valence band (VB) and conduct band (CB) of TiO₂, C-TiO₂ and g-C₃N₄ are determined by UV-vis DRS and VB-XPS. From Fig. 10a, it can be known that the corresponding band gaps of TiO₂, C-TiO₂ and g-C₃N₄ are 3.18 eV, 2.73 eV and 2.65 eV, respectively. The band gap of the C-TiO₂ is estimated with a decrease of 0.45 eV, which is mainly attributed to C doping into the interstitial sites. Fig. 10b shows valence band XPS (VB-XPS) for the TiO₂, C-TiO₂ and g-C₃N₄. It indicates the VB of TiO₂ occurs at 2.74 eV. The VB edge of C-TiO₂ is at 2.29 eV, shifts toward negative energy than that of TiO₂, meaning that the VB top of C-TiO₂ is indeed lifted up which is caused by the contribution of C 2p orbitals [38,39]. Therefore, their corresponding CB should be located at -0.45 eV. The VB of g-C₃N₄ is revealed to be 1.71 eV, and the CB is calculated to be

0.94 eV. So this heterojunction structure of C-TiO₂/g-C₃N₄ is benefit for the separation of electron-hole pair.

3.6. PL and time-resolved PL spectral analyses

Fig. 11 shows the PL spectra of all samples. The samples are excited at 325 nm. The highest PL emission intensity is presented in the g-C₃N₄ sample, indicating that the recombination of electron-hole pairs is the most severe. Obviously, the PL intensity decreases sharply after coupling with C-TiO₂, as shown in Fig. 11. This is attributed to the formation of heterojunction between C-TiO₂ and g-C₃N₄, which accelerates the electron-hole pair separation. Moreover, the PL intensity becomes weaker with the increase of g-C₃N₄ in the C-TiO₂/g-C₃N₄ nanocomposite. Besides, it suddenly intensifies when the mass of g-C₃N₄ is 0.1 g. Because g-C₃N₄ dominates in the composition, the finite heterojunction limits the separation of charges. Similarity, the low addition of g-C₃N₄ is unable to generate enough heterojunctions to aid charge separation. However,

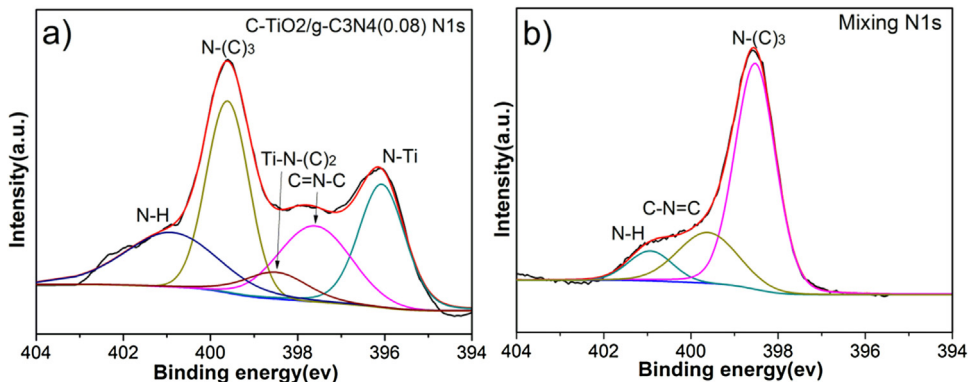


Fig. 7. N 1s high resolution XPS spectra of C-TiO₂/g-C₃N₄(0.08) (a) and the Mixing sample (b).

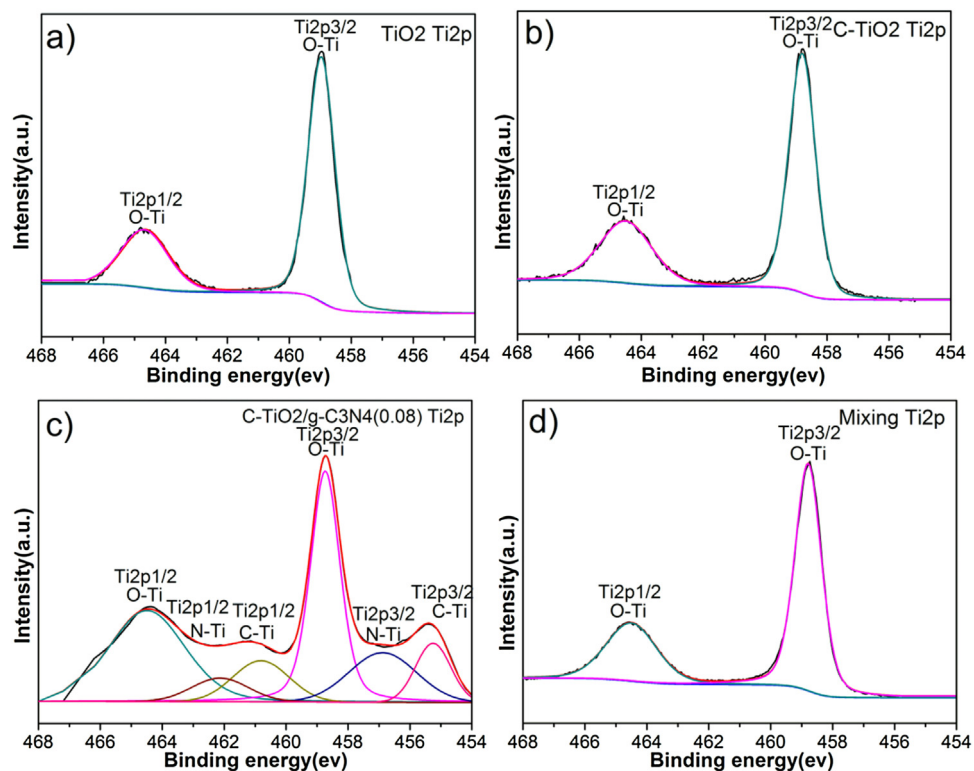


Fig. 8. Ti 2p high resolution XPS spectra of TiO₂ (a), C-TiO₂ (b), C-TiO₂/g-C₃N₄(0.08) (c) and the Mixing sample (d).

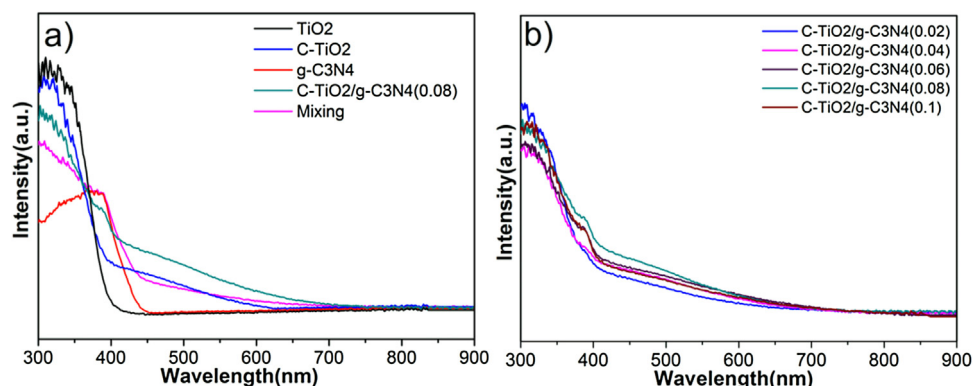


Fig. 9. UV-vis DRS of all samples.

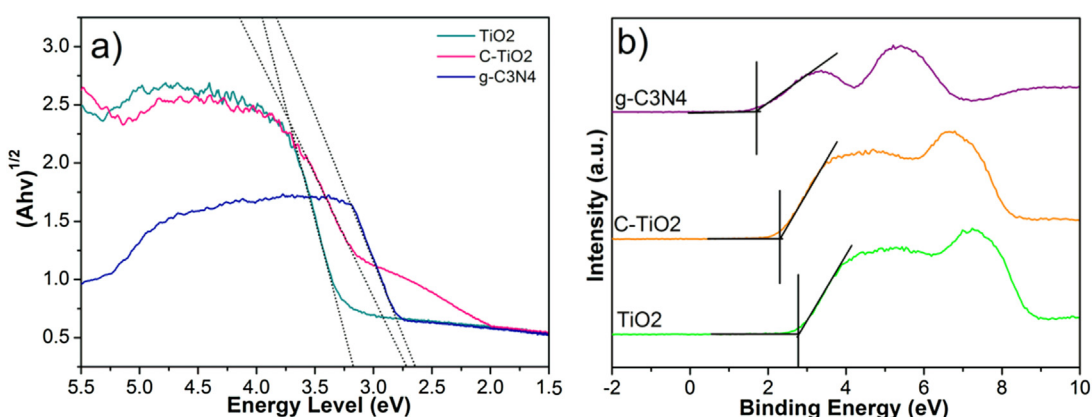


Fig. 10. Estimated band gaps (a); VB XPS spectra of TiO₂, C-TiO₂ and g-C₃N₄ (b).

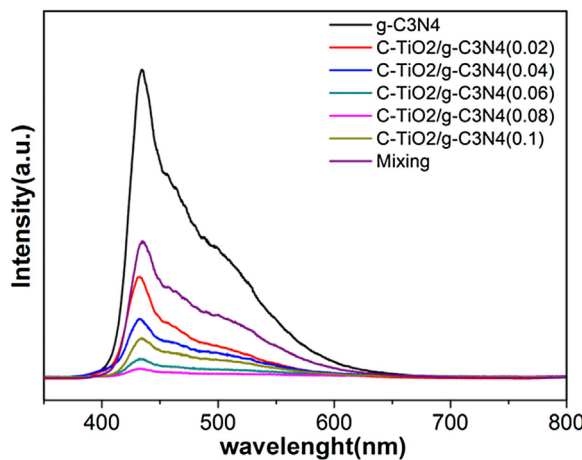


Fig. 11. PL spectra of all samples.

PL intensity of the Mixing sample is higher than those of all C-TiO₂/g-C₃N₄ nanocomposites; this could be caused by the poorer separation of electron-hole pairs.

To further depict the charge transfer of all samples, time-resolved PL spectra is shown in Fig. 12. Generally, the shorter lifetime is associated with the recombination of the electron-hole pairs, while the longer lifetime is attributed to fast separation of electron-hole pairs [40,41]. By multi-exponential fitting, values of the calculated decay time constant are shown in Table S1. For the decay curves of all samples, it can be seen that the lifetimes of the photogenerated charge carriers on all nanocomposites and the Mixing sample are slightly prolonged compared with each single component, which are consequently favorable for interfacial electron transfer after the construction of heterojunction. However, the C-TiO₂/g-C₃N₄(0.08) has a longer lifetime compared with the Mixing sample, confirming that relatively better photogenerated carriers separation. This explains that the interfacial charge transfer through C—Ti bond and N—Ti bond plays an important role in facilitating the separation of electron-hole pairs. When the ratio of g-C₃N₄ to C-TiO₂ increases gradually, the τ increases first and decreases then, the result is accord with PL spectrum.

3.7. Photoelectrochemical measurements

To further investigate and understand the excitation and transfer of photogenerated charge carriers of all as-prepared samples, the photocurrent response (J-t) experiments shown in Fig. 13 were

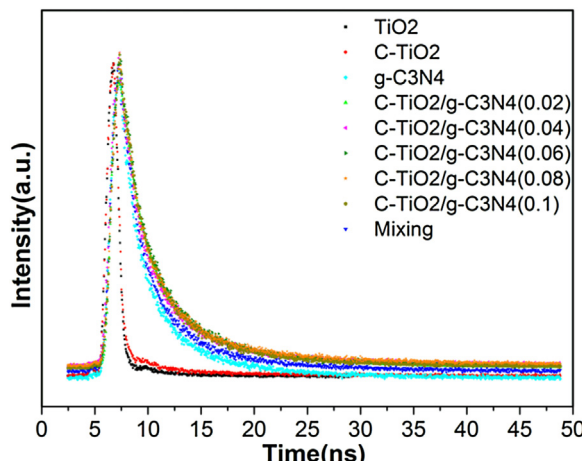
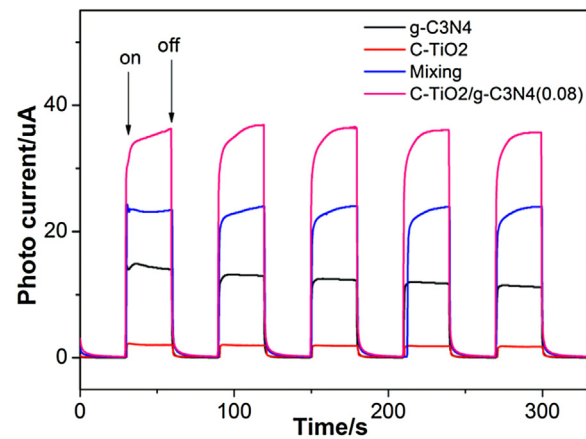


Fig. 12. Time-resolved PL spectra of all samples monitored at 500 nm.

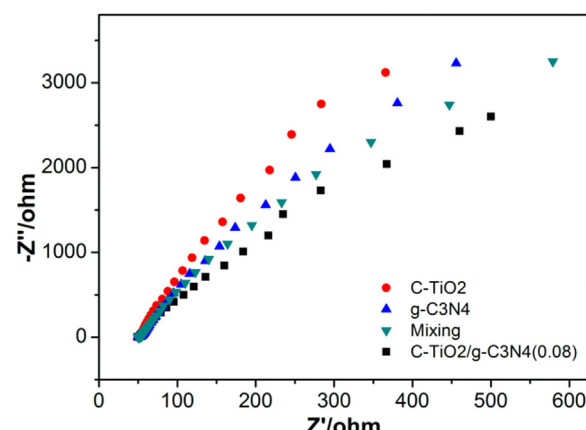
Fig. 13. Transient photocurrent responses of C-TiO₂, g-C₃N₄, C-TiO₂/g-C₃N₄(0.08) and the Mixing sample under visible light.

performed. It can be observed that all samples possess a relatively stable photocurrent response. The transient photocurrent density obtained over the C-TiO₂/g-C₃N₄(0.08) is obviously higher than that of C-TiO₂ and g-C₃N₄ severally. Photocurrent density of the Mixing sample is also enhanced compared to that of each single component, but lower than that of the C-TiO₂/g-C₃N₄(0.08). It can be seen clearly that C-TiO₂/g-C₃N₄(0.08) possesses the highest photocurrent, indicating it has the most effective separation and the longest lifetime of the photogenerated electrons. And it is mainly due to the effective interfacial charge transfer through the chemical interactions and the synergistic effect of C-TiO₂ nanoparticles and g-C₃N₄ nanosheets.

As shown in Fig. 14, EIS Nyquist analysis was performed to further investigate the interfacial electron transfer. Since the radius of each arc is related to the charge transfer process at the electrode/electrolyte interface, it suggests that the C-TiO₂/g-C₃N₄(0.08) has a more effective separation of photogenerated electron-hole pairs and faster interfacial electron transfer. The result also indicates that chemical combination of C-TiO₂ and g-C₃N₄ is benefit to electron transfer, which agrees well with the result of the transient photocurrent responses.

3.8. Electron spin resonance spectra

To confirm the roles of $\cdot\text{O}_2^-$ and $\cdot\text{OH}$ during photocatalytic process, ESR spectra of C-TiO₂/g-C₃N₄(0.08) were performed using DMPO as radical trapper under visible light irradiation. As shown in

Fig. 14. Electrochemical impedance spectroscopy of C-TiO₂, g-C₃N₄, C-TiO₂/g-C₃N₄(0.08) and the Mixing sample.

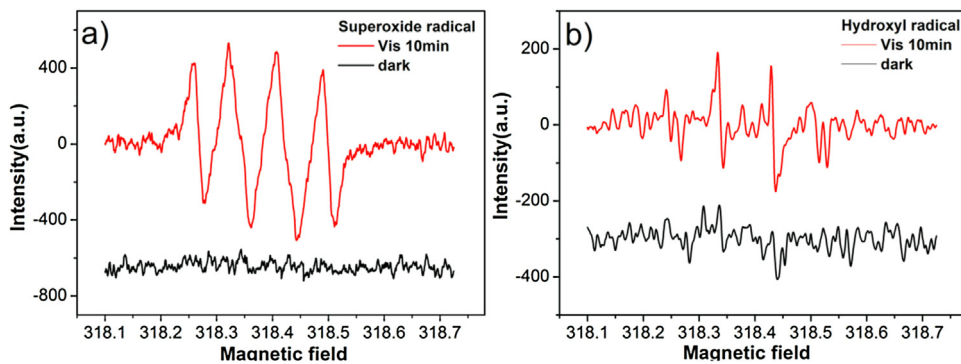


Fig. 15. ESR spectra of C-TiO₂/g-C₃N₄(0.08) in aqueous solution before and after visible light irradiation: (a) DMPO-•O₂⁻ and (b) DMPO-•OH.

Fig. 15a and b, no signals are detected in the dark. After 10 min visible light irradiation, the characteristic signals of the DMPO-•O₂⁻ (Fig. 15a) and DMPO-•OH (Fig. 15b) are both observed obviously. The signal of •O₂⁻ is much stronger than that of •OH under visible light. Because the holes transferred from the valence band (VB) of C-TiO₂ to the VB of g-C₃N₄ once the heterojunction formed, however, VB of g-C₃N₄ is -1.40 eV, cannot directly oxidize H₂O or OH⁻ into •OH radicals (E^0 (H₂O/•OH) = 2.40 V, E^0 (OH⁻/•OH) = 1.99 V). So a small number of •OH radicals could be generated from the following reaction: •O₂⁻ + e⁻ + 2H⁺ → H₂O₂, H₂O₂ + e⁻ → •OH + OH⁻. Thus it can be seen that •O₂⁻ is the main active species.

3.9. Photocatalytic activity

Fig. 16a displays the photocatalytic properties of all samples based on the degradation of MO under visible light irradiation. The results indicate that the pure TiO₂ has no catalytic activity under visible light irradiation, and the photocatalytic activities are greatly improved by the doping of carbon. Moreover, all C-TiO₂/g-C₃N₄ nanocomposites exhibit excellent photocatalytic activities

which are all higher than that of single component. When the mass ratio of C-TiO₂/g-C₃N₄ is 27:8 (C-TiO₂/g-C₃N₄(0.08)), the photocatalytic activity is the best and the MO removal reaches about 98.6% after 1 h reaction. Compared with the C-TiO₂/g-C₃N₄(0.08), the Mixing sample exhibits a poorer photocatalytic activity and the photodegradation rate of MO only reaches about 69.65%. In order to clarify the superiority of the C-TiO₂/g-C₃N₄(0.08), the results of the comparison with the reported photocatalysts have been shown in Table S2. It indicates that the C-TiO₂/g-C₃N₄(0.08) really exhibits great visible light photocatalysis performance.

The photocatalysis degradation follows the first-order kinetics. The kinetics can be expressed as follows: $-\ln(C/C_0) = k_{app}t$. Fig. 16b presents the linear relationship between $\ln(C/C_0)$ and time, where C/C_0 is the normalized as MO concentration, t is the reaction time, and k is the reaction rate constant (10^{-3} min^{-1}). Fig. 16c displays the reaction rate constants of all samples. The rate constant of C-TiO₂/g-C₃N₄(0.08) is calculated to be 0.0448 min^{-1} , which is about 5.1, 3.8 and 2.3 times higher than that of C-TiO₂, g-C₃N₄ and the Mixing sample respectively. Therefore, it is convincing that the construction of a heterojunction structure with effective

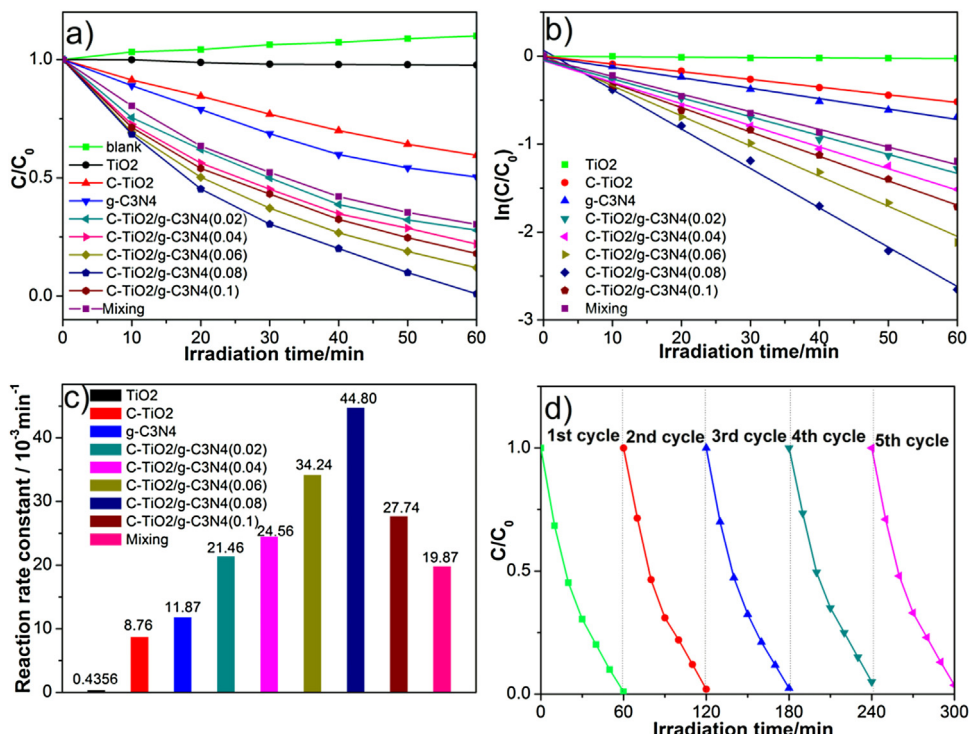


Fig. 16. (a) photodegradation rate of MO under visible light illuminated for 1 h on all samples; (b) kinetic curves for the photocatalytic degradation of all samples; (c) reaction rate constant of all samples; (d) stability study for the photocatalytic MO degradation by C-TiO₂/g-C₃N₄(0.08).

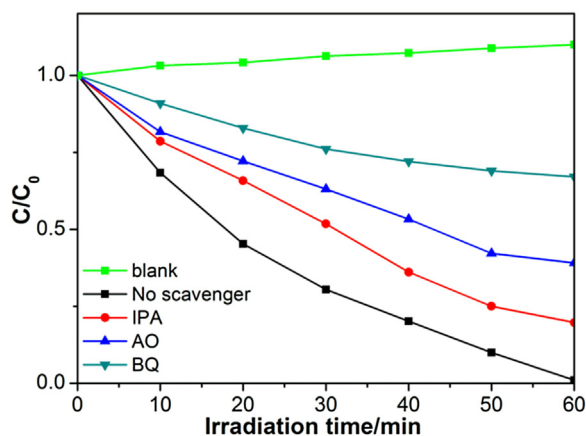


Fig. 17. Photodegradation rate of MO after different scavengers were added.

separation of electron-hole pairs through chemically bond connection as a visible light photocatalyst can enhance photocatalytic activities drastically.

For the practical application of photocatalysts, the stability of photocatalyst is one of the key issues. The by-products are always adsorbed on the surface-active position of the photocatalyst. The photocatalytic activity will decrease dramatically after a short period of exposure time. To evaluate the stability of as-prepared C-TiO₂/g-C₃N₄(0.08), recycle experiments under same conditions were conducted. According results shown in Fig. 16d, the C-TiO₂/g-C₃N₄(0.08) still exhibits superb catalytic performance in the fifth cycle.

To further explore the role of active species photogenerated in the reaction process, relevant scavengers are added to the MO solution through contrasting variation of degradation rate. As shown in Fig. 17, it clearly reveals that the degradation rate remarkably decreases after adding IPA, AO and BQ. And the degradation rate follows the order: No scavenger > IPA > AO > BQ. Therefore, it can be known that h⁺, O₂[−], OH as active species are generated in the photocatalytic reaction and O₂[−] plays a significantly important role.

3.10. Mechanism discussion

Based on the above analysis and discussion, it can be concluded that chemically bonded interfacial contact between C-TiO₂ and g-C₃N₄ and the improvement of light harvesting are major factors for improving the photo-electrochemical performance and photocatalytic activity. As illustrated in Fig. 18, when the C-TiO₂/g-C₃N₄ nanocomposite is irradiated by visible light, electrons are excited from the VB to the CB of C-TiO₂ and g-C₃N₄, leaving holes in the VB. Due to the CB of g-C₃N₄ lies rather higher than C-TiO₂, and the VB for g-C₃N₄ is located at a higher position than C-TiO₂, the excited electrons transfer from the CB of g-C₃N₄ to the CB of C-TiO₂ while the holes migrate in the opposite direction. Moreover, the g-C₃N₄ loading with C-TiO₂ with intimate chemically bonded (C-Ti bond and N-Ti bond) interfaces can be benefit for charge transport, hinder the recombination of electron-hole pairs and further increase the number of charge carrier in the reaction. Meanwhile, the C-TiO₂/g-C₃N₄ nanocomposite exhibits the strongest visible light absorption. And it is attributed to the narrowed gap which is caused by the migration of electrons and holes. So the chemically bonded C-TiO₂/g-C₃N₄ composite exhibits better photocatalytic activity.

On the basis of the ESR spectra and scavenger experiments, combined with the above mechanism analysis, the O₂[−] is main role in the photocatalytic reaction generated from the reduction of

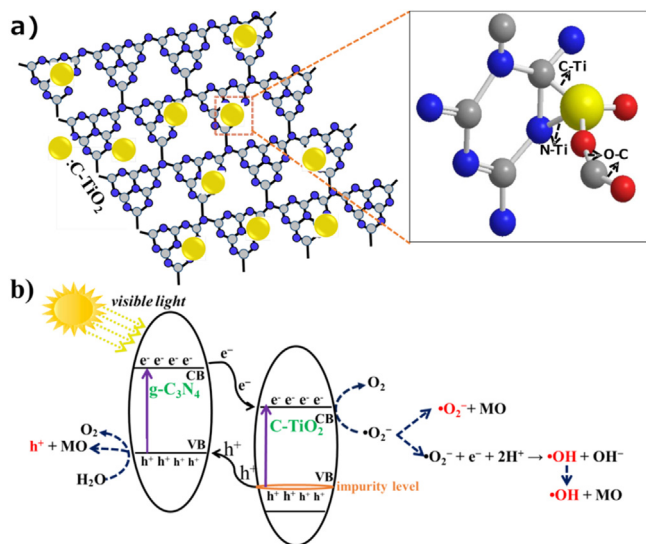
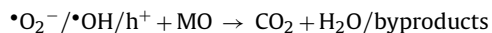
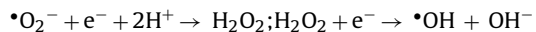
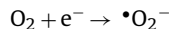
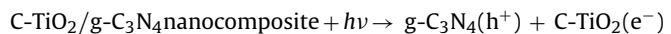


Fig. 18. Schematic illustrations for chemically bonded C-TiO₂/g-C₃N₄ nanocomposite (a) and photocatalytic process (b).

O₂ in the CB of C-TiO₂. And the VB of g-C₃N₄ is -1.40 eV , cannot directly oxidize H₂O or OH[−] into OH radicals, the OH is produced from the further reaction of O₂[−], e[−] and 2H⁺. Photocatalytic process is shown in Fig. 18b and can be expressed by the following procedures.



4. Conclusions

In conclusion, C-TiO₂/g-C₃N₄ nanocomposite with high photocatalytic activity was successfully synthesized by a facile hydrothermal method. And the optimum mass ratio of g-C₃N₄ to C-TiO₂ was 27:8. TEM revealed that C-TiO₂ nanoparticles were well grown on the g-C₃N₄ nanosheets surfaces. UV-vis spectra show that it exhibits the strongest visible light absorption. XPS indicated that the C-TiO₂ nanoparticles were chemically bonding with the g-C₃N₄ nanosheets, which was confirmed by the formation of the C-Ti bond and N-Ti bond. This chemical bond combination structure was beneficial for the formation of effective heterojunction, which could result in a synergistic combination of C-TiO₂ and g-C₃N₄ that significantly decreased the recombination of electron-hole pairs and enhanced separation of photogenerated carrier. It was also demonstrated by the photocurrent response experiment, the electrochemical impedance spectroscopy measurements, PL spectra and Time-resolved PL spectra. Moreover, ESR spectra and scavengers experiments both revealed that O₂[−] was the main role participating in the photocatalytic activity.

Acknowledgement

This work was financially supported by Innovation Foundation of Graduate Innovation and Entrepreneurship Base of Huazhong University of Science and Technology (No. 2015650011) and the National Basic Research Program of China (Grant Nos.

2009CB939705). The authors are also grateful to Analytic and Testing Center of Huazhong University of Science and Technology.

Appendix A. Supplementary data

Supplementary data associated with this article can be found, in the online version, at <http://dx.doi.org/10.1016/j.apcatb.2016.09.052>.

References

- [1] S.D. Perera, R.G. Mariano, K. Vu, N. Nour, O. Seitz, Y. Chabal, K.J. Balkus, *ACS Catal.* 2 (2012) 949–956.
- [2] Y. Huo, J. Zhang, M. Miao, Y. Jin, *Appl. Catal. B—Environ.* 111–112 (2012) 334–341.
- [3] Y. Tian, B. Chang, J. Lu, J. Fu, F. Xi, X. Dong, *ACS Appl. Mater. Interfaces* 5 (2013) 7079–7085.
- [4] L. Pan, J.-J. Zou, X. Zhang, L. Wang, *J. Am. Chem. Soc.* 133 (2011) 10000–10002.
- [5] F. Akira, *Nature* 238 (1972) 37–38.
- [6] X. Chen, C. Burda, *J. Am. Chem. Soc.* 130 (2008) 5018–5019.
- [7] I. Robel, V. Subramanian, M. Kuno, P.V. Kamat, *J. Am. Chem. Soc.* 128 (2006) 2385–2393.
- [8] N. Zhang, S. Liu, X. Fu, Y.-J. Xu, *J. Phys. Chem. C* 115 (2011) 9136–9145.
- [9] L.L. Xiaobo Chen, Peter Y. Yu, Samuel S. Mao, *Science* 331 (2011) 746–750.
- [10] X.-X. Wei, H. Cui, S. Guo, L. Zhao, W. Lia, *J. Hazard. Mater.* 263 (2013) 650–658.
- [11] Y. Xie, G. Ali, S.H. Yoo, S.O. Cho, *ACS Appl. Mater. Interfaces* 2 (2010) 2910–2914.
- [12] Y. Wang, Y.-n. Zhang, G. Zhao, H. Tian, H. Shi, T. Zhou, *ACS Appl. Mater. Interfaces* 4 (2012) 3965–3972.
- [13] W. Zhou, H. Liu, J. Wang, D. Liu, G. Du, J. Cui, *ACS Appl. Mater. Interfaces* 2 (2010) 2385–2392.
- [14] L. Gu, J. Wang, Z. Zou, X. Han, *J. Hazard. Mater.* 268 (2014) 216–223.
- [15] Y. Chen, W. Huang, D. He, Y. Situ, H. Huang, *ACS Appl. Mater. Interfaces* 6 (2014) 14405–14414.
- [16] Z. Sheng, L. Ying, L. Jianmei, W. Yajun, J. Guiyuan, Z. Zhen, W. Daxi, D. Aijun, L. Jian, W. Yuechang, *Appl. Catal. B—Environ.* 158–159 (2014) 20–29.
- [17] K. Sridharan, E. Jang, T.J. Park, *Appl. Catal. B—Environ.* 142–143 (2013) 718–728.
- [18] W. Ren, Z. Ai, F. Jia, L. Zhang, X. Fan, Z. Zou, *Appl. Catal. B—Environ.* 69 (2007) 138–144.
- [19] X. Yang, C. Cao, L. Erickson, K. Hohn, R. Maghirang, K. Klabunde, *Appl. Catal. B—Environ.* 91 (2009) 657–662.
- [20] Q. Liang, Z. Li, X. Yu, Z.-H. Huang, F. Kang, Q.-H. Yang, *Adv. Mater.* 27 (2015) 4634–4639.
- [21] S.C. Yan, Z.S. Li, Z.G. Zou, *Langmuir* 25 (2009) 10397–10401.
- [22] Z.a. Huang, Q. Sun, K. Lv, Z. Zhang, M. Li, B. Li, *Appl. Catal. B—Environ.* 164 (2015) 420–427.
- [23] J. Wang, J. Huang, H. Xie, A. Qu, *Int. J. Hydrogen Energy* 39 (2014) 6354–6363.
- [24] X. Zhang, X. Xie, H. Wang, J. Zhang, B. Pan, Y. Xie, *J. Am. Chem. Soc.* 135 (2013) 18–21.
- [25] X. Zhang, H. Wang, H. Wang, Q. Zhang, J. Xie, Y. Tian, J. Wang, Y. Xie, *Adv. Mater.* 26 (2014) 4438–4443.
- [26] P. Niu, L. Zhang, G. Liu, H.-M. Cheng, *Adv. Funct. Mater.* 22 (2012) 4763–4770.
- [27] O. Akhavan, M. Abdolahad, Y. Abdi, S. Mohajerzadeh, *Carbon* 47 (2009) 3280–3287.
- [28] H.-N. Kim, H. Yoo, J.H. Moon, *Nanoscale* 5 (2013) 4200–4204.
- [29] Z. Lei, S. Wulin, L. Minghui, Z. Dawen, X. Changsheng, *Appl. Catal. B—Environ.* 147 (2014) 490–498.
- [30] S.C. Yan, Z.S. Li, Z.G. Zou, *Langmuir* 26 (2010) 3894–3901.
- [31] F. Dong, S. Guo, H. Wang, X. Li, Z. Wu, *J. Phys. Chem. C* 115 (2011) 13285–13292.
- [32] L. Zhang, R.V. Koka, *Mater. Chem. Phys.* 57 (1998) 23–32.
- [33] Q. Huang, S. Tian, D. Zeng, X. Wang, W. Song, Y. Li, W. Xiao, C. Xie, *ACS Catal.* 3 (2013) 1477–1485.
- [34] L. Ge, C. Han, *Appl. Catal. B—Environ.* 117–118 (2012) 268–274.
- [35] B. Avasarala, P. Haldar, *Electrochim. Acta* 55 (2010) 9024–9034.
- [36] L. Zeng, Z. Lu, M. Li, J. Yang, W. Song, D. Zeng, C. Xie, *Appl. Catal. B—Environ.* 183 (2016) 308–316.
- [37] T. Lin, C. Yang, Z. Wang, H. Yin, X. Lü, F. Huang, J. Lin, X. Xie, M. Jiang, *Energy Environ. Sci.* 7 (2014) 967–972.
- [38] Z. Wu, F. Dong, W. Zhao, H. Wang, Y. Liu, B. Guan, *Nanotechnology* 20 (2009) 235701.
- [39] F. Dong, H. Wang, G. Sen, Z. Wu, S.C. Lee, J. Hazard. Mater. 187 (2011) 509–516.
- [40] C. Ye, J.-X. Li, Z.-J. Li, X.-B. Li, X.-B. Fan, L.-P. Zhang, B. Chen, C.-H. Tung, L.-Z. Wu, *ACS Catal.* 5 (2015) 6973–6979.
- [41] X. She, L. Liu, H. Ji, Z. Mo, Y. Li, L. Huang, D. Du, H. Xu, H. Li, *Appl. Catal. B—Environ.* 187 (2016) 144–153.